PHYSICAL REVIEW A **81**, 052502 (2010)

Initial-state dependence of coupled electronic and nuclear fluxes in molecules

A. Kenfack,[1] F. Marquardt,[2,3] G. K. Paramonov,[1] I. Barth,[1] C. Lasser,[3] and B. Paulus[1]
[1]*Physikalische und Theoretische Chemie, Institut für Chemie und Biochemie, Freie Universität Berlin, D-14195 Berlin, Germany*
[2]*Visualization and Data Analysis, Zuse Institute Berlin, D-14195 Berlin, Germany*
[3]*Fachbereich Mathematik, Freie Universität Berlin, D-14195 Berlin, Germany*
(Received 12 February 2010; published 6 May 2010)

We demonstrate that coupled electronic and nuclear fluxes in molecules can strongly depend on the initial state preparation. Starting the dynamics of an aligned $D_2{}^+$ molecule at two different initial conditions, the inner and the outer turning points, we observe qualitatively different oscillation patterns of the nuclear fluxes developing after 30 fs. This corresponds to different orders of magnitude bridged by the time evolution of the nuclear dispersion. Moreover, there are attosecond time intervals within which the electronic fluxes do not adapt to the nuclei motion depending on the initial state. These results are inferred from two different approaches for the numerical flux simulation, which are both in good agreement.

DOI: 10.1103/PhysRevA.81.052502 PACS number(s): 31.50.Bc, 82.20.Bc, 82.20.Wt

I. INTRODUCTION

In the course of a chemical reaction, the making and the breaking of bonds is regulated by the correlated motion of electrons and nuclei. Recent advances in laser technology allow the resolution of electronic dynamics on attosecond time scales [1–8] and strongly suggest the theoretical investigation of combined nuclear and electronic motion in molecules.

During the past few decades chemical reaction rates have successfully been approached via nuclear flux computations [9–11]. Only recently have two complementary methods for the evaluation of coupled molecular quantum fluxes been proposed [12,13]. In Ref. [12], Okuyama *et al.* use the Ehrenfest theorem for computing electronic fluxes. In Ref. [13], Barth *et al.* start from the time-dependent Born-Oppenheimer approximation and infer approximate electronic and nuclear fluxes via Gauss's divergence theorem.

Here we follow the approach developed in Ref. [13] and explore coupled nuclear and electronic fluxes, focusing on their dependence on the initial state. Our theoretical investigations are partly motivated by recent experiments on N_2O_4 [14]. There, strong higher harmonics are generated depending on whether the pump pulse excites the vibrational ground state to the inner or the outer turning point. At this point, the question that may naturally arise is what would be the impact of a comparable initial preparation at the molecular flux level? To the best of our knowledge, such an investigation has not yet been considered.

Our working example is the deuterium molecular ion $D_2{}^+$, which is chosen as a prototype for the future investigation of more complex molecules. Here we demonstrate that the time-evolution of coupled molecular fluxes strongly depends on the initial state preparation and is qualitatively different, when starting on the inner or the outer turning point. When the initial wave function is set at the inner turning point, the nuclear fluxes form pronounced oscillations after 30 fs, which is not the case for the outer initial state. This difference corresponds to different orders of magnitude bridged by the time evolution of the nuclear dispersion. Moreover, the initial state affects the synchronicity as well as the directionality of both nuclear and electronic fluxes. There are attosecond time intervals within which the electronic fluxes do not follow the nuclear ones. The robustness of these phenomena with respect to the position of the observer is shown, and numerical results are confirmed by simulations for the time-dependent Schrödinger equation with explicit dependence on electronic and nuclear degrees of freedom. All these results complement considerably the findings of our earlier application on $H_2{}^+$ in which the initial condition is exclusively set at the outer turning point [13].

The article is organized as follows. In Sec. II our model of $D_2{}^+$ is described together with the preparation of the initial states. Sec. III defines the electronic and nuclear fluxes and discusses their computation via the Born-Oppenheimer approximation. In Sec. IV we present the time evolution of the fluxes and discuss the obtained results, especially the differences with respect to the oscillation pattern and the synchronicity of electronic and nuclear fluxes. Section V summarizes and concludes the present work. The appendix collects details of the numerical simulations.

II. THE MODEL AND INITIAL STATES

Our model of the deuterium molecular ion $D_2{}^+$ in the electronic ground state $1s\sigma_g$ consists of one-dimensional motion of the nuclei and two-dimensional motion of the electron. It is aimed at vibrational processes occuring on the femtosecond time scale, which is much earlier than the slower rotational time scale of the molecule.

One describes the electron in cylindrical coordinates $(r\cos\phi, r\sin\phi, z)$ and assumes that the nuclei localize along the electronic z axis for the time scale of interest. Consequently, nuclear motion is described by the internuclear distance R alone. This allows to eliminate the electronic angular variable ϕ, and only three spatial degrees of freedom (r, z, R) are left for the dynamics. Then, the time-dependent Schrödinger equation can be written as ($m_e = \hbar = e = 1$)

$$i\frac{\partial}{\partial t}\Psi(r,z,R,t) = \mathcal{H}\Psi(r,z,R,t) \tag{1}$$

with

$$\mathcal{H} = T_e + T_n + V_{nn} + V_{en}$$

the molecular Hamiltonian and $\Psi(r,z,R,t)$ the total wave function of the electron and the nuclei. Here,

$T_n = -1/(2\mu_n)\partial^2/\partial R^2$ is the kinetic energy of the nuclei with the reduced mass $\mu_n = m_d/2 = 1836$ au, $V_{nn} = 1/R$ the nuclei-nuclei interaction,

$$T_e = -\frac{1}{2\mu_e}\frac{\partial^2}{\partial z^2} - \frac{1}{2\mu_e}\left(\frac{\partial^2}{\partial r^2} + \frac{1}{r}\frac{\partial}{\partial r}\right),$$

the electronic kinetic energy with $1/\mu_e = 1 + 1/(2m_d)$, and

$$V_{en} = -\frac{1}{\sqrt{r^2 + (z - R/2)^2}} - \frac{1}{\sqrt{r^2 + (z + R/2)^2}},$$

the electron-nuclei interaction.

Our initial state is the Born-Oppenheimer wave function

$$\Psi(r,z,R,t = 0) = \Psi_n(R,t = 0)\Psi_e(r,z;R). \tag{2}$$

The nuclear wave function $\Psi_n(R,0)$ is the ground state of the neutral molecule D_2, promoted to $D_2{}^+$ $(1s\sigma_g)$; while the electronic wave function $\Psi_e(r,z;R)$ is the $1s\sigma_g$ electronic wavefunction of $D_2{}^+$ parametrized by the internuclear distance R. Details on the preparation of our initial states can be found in the appendix.

Figure 1 illustrates this setup. Figure 1(a) shows the potential energy surface $V(R)$ of $D_2{}^+$ together with the two different initial states of our dynamics. The regions (1) and (2) correspond to the outer and inner turning points with respect to the equilibrium internuclear distance $R_{\mathrm{eq}} = 2.0a_0$. The center of the nuclear wave packet $\Psi_n(R,0)$ is chosen as $R_1 = 3.125a_0$ and $R_2 = 1.5a_0$, respectively. The energies of the associated states are identical and equal to $E = -0.575$ a.u.. In Fig. 1(b), the acting force $K = -dV/dR$ clearly shows that the nuclear wave packet is driven more strongly in the inner region (2) than in the outer region (1). A more detailed discussion of the influence of this force on the nuclear dispersion is provided in subsection IV B.

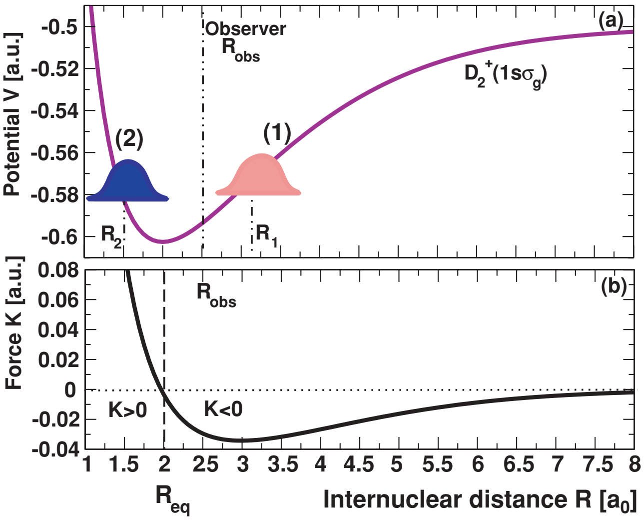

FIG. 1. (Color online) (a) The potential energy surface $V(R)$ of $D_2{}^+$. The outer (1) and the inner (2) regions denote the initial locations of the nuclear wave packets centered at R_1 and R_2, respectively. These wave packets have been promoted to $D_2{}^+$ from the ground state of D_2. The dot-dashed vertical lines indicate the location of our observer R_{obs}. (b) The force $K = -dV/dR$ acting on the nuclear wave packet. The equilibrium internuclear distance R_{eq} is indicated by a dashed vertical line.

III. THE FLUXES

From the total wave function $\Psi(r,z,R,t)$ one derives the continuity equation for the total density $\rho_{\mathrm{tot}}(r,z,R,t) = |\Psi(r,z,R,t)|^2$:

$$\dot{\rho}_{\mathrm{tot}}(r,z,R,t) = -\nabla\cdot\mathbf{j}(r,z,R,t). \tag{3}$$

The total current density is

$$\mathbf{j} = \begin{pmatrix} \frac{1}{\mu_e}\mathrm{Im}(\Psi^*\nabla_e\Psi) \\ \frac{1}{\mu_n}\mathrm{Im}(\Psi^*\nabla_n\Psi) \end{pmatrix},$$

where the gradient in nuclear and in electronic coordinates is denoted by ∇_n and ∇_e, respectively.

A. The electronic flux

We turn to the electronic density

$$\rho_e(r,z,t) = \int dR|\Psi(r,z,R,t)|^2. \tag{4}$$

Integrating the full continuity equation, Eq. (3), over the nuclear degrees of freedom, one obtains the reduced continuity equations for the electrons

$$\dot{\rho}_e(r,z,t) = -\nabla_e\cdot\mathbf{j}_e(r,z,t), \tag{5}$$

where

$$\mathbf{j}_e = \frac{1}{\mu_e}\int dR\ \mathrm{Im}(\Psi^*\nabla_e\Psi) \tag{6}$$

is the electronic current density. We are interested in monitoring the flux through the observer surface A_{obs}, which is the boundary of a subset of the volume V_{obs}. This is given by the surface integral

$$F_e(t;A_{\mathrm{obs}}) = -\int_{A_{\mathrm{obs}}} d\mathbf{A}\cdot\mathbf{j}_e. \tag{7}$$

Following Barth *et al.* [13], we use the divergence theorem together with the electronic continuity equation, Eq. (5), to rewrite the flux in terms of the density,

$$F_e(t;A_{\mathrm{obs}}) = \frac{d}{dt}\int_{V_{\mathrm{obs}}} dV\rho_e. \tag{8}$$

Integrating over the time interval $[0,t]$ we obtain the associated electronic yield

$$Y_e(t;A_{\mathrm{obs}}) = \int_0^t d\tau\, F_e(\tau;A_{\mathrm{obs}}). \tag{9}$$

In our model system, the surface of observation is defined by two planes parallel to the plane $z = 0$ with distance R_{obs}, i.e., $z_{\mathrm{obs}} = \pm R_{\mathrm{obs}}/2$, as illustrated in Fig. 2. Therefore, in the associated observing volume V_{obs}, the electronic flux can be expressed as

$$F_e(t;A_{\mathrm{obs}}) = \frac{d}{dt}\int_0^\infty rdr\int_{-z_{\mathrm{obs}}}^{z_{\mathrm{obs}}} dz\rho_e(r,z,t). \tag{10}$$

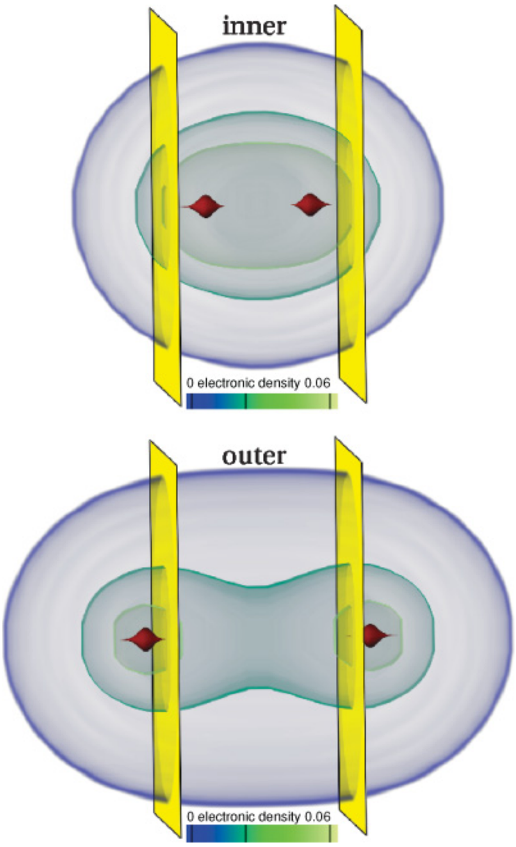

FIG. 2. (Color online) Visualization of the initial states as defined in Fig. 1. The upper panel represents the inner initial state and the lower panel the outer one. The electronic density, with its associated color code, surrounds the nuclear densities in red (dark gray). The space inside the two parallel planes of the observer A_{obs}, in yellow (light gray), corresponds to the volume of the observer V_{obs}. The two planes are located at $z_{\mathrm{obs}} = \pm R_{\mathrm{obs}}/2$, where R_{obs} is the distance separating the two planes. This visualization has been created using the academic system ZIBAMIRA, a superset of its commercial version AMIRA [15].

The observer position R_{obs} should allow to monitor maximum fluxes for both sets of initial states. Therefore we have chosen $R_{\mathrm{obs}} = 2.5a_0$.

B. The BO approximation

One way for computing the electronic and the nuclear fluxes is the numerical solution of the time-dependent molecular Schrödinger equation, Eq. (1). The state-of-the-art methods [16,17], which treat this problem in full dimensionality, are still restricted to three-body problems such as our working model, although few extensions to larger systems have been proposed [4,18,19]. In general, however, the Born-Oppenheimer (BO) approximation [20] proposed in 1927 is still indispensable.

The BO approximation is based on the large ratio between nuclear and electronic masses. The nuclei are thus slower, thereby allowing the approximation of their dynamics by an effective equation of motion with averaged electronic degrees of freedom, while the electronic averaging process works with the nuclei frozen in a given configuration. It basically allows to break the wave function of a molecule in its electronic and nuclear components. For our model, the total wave function $\Psi(r,z,R,t)$ is approximated by the BO wave function

$$\Psi_{\mathrm{BO}}(r,z,R,t) = \Psi_n(R,t)\Psi_e(r,z;R). \tag{11}$$

The electronic wave function $\Psi_e(r,z;R)$, which depends parametrically on the nuclear degree of freedom R, is the solution of the time-independent electronic Schrödinger equation

$$\mathcal{H}_e\Psi_e(r,z;R) = V(R)\Psi_e(r,z;R) \tag{12}$$

with $\mathcal{H}_e = T_e + V_{nn} + V_{en}$ the electronic Hamiltonian and $V(R)$ the Potential Energy Surface (PES). The nuclear wave function $\Psi_n(R,t)$ is the solution of the time-dependent nuclear Schrödinger equation

$$i\frac{\partial}{\partial t}\Psi_n(R,t) = [T_n + V(R)]\Psi_n(R,t). \tag{13}$$

We note that the electronic wave function is the electronic ground state of $D_2{}^+$ which is indeed real valued. This makes it problematic to use of the BO approximation for the computation of the gradient of the total wave function. Specifically the electronic current density is zero, see Eq. (6), in contrast to what one would expect. Therefore we do not employ the current density $\mathbf{j}_e$ but instead the density ρ_e to compute the fluxes via the density formulation, Eq. (8).

C. The nuclear flux

For the derivation of the nuclear flux we proceed similarly as for the electronic one. We define the nuclear density

$$\rho_n(R,t) = \int dz\, r\, dr|\Psi(r,z,R,t)|^2. \tag{14}$$

It satisfies the reduced continuity equation

$$\dot{\rho}_n(R,t) = -\nabla_n \cdot \mathbf{j}_n(R,t) \tag{15}$$

with the nuclear current density

$$\mathbf{j}_n = \frac{1}{\mu_n}\int dz\, r\, dr \mathrm{Im}(\Psi^*\nabla_n\Psi).$$

The nuclear flux through the surface A_{obs} is

$$F_n(t;A_{\mathrm{obs}}) = -\int_{A_{\mathrm{obs}}} d\mathbf{A}\cdot\mathbf{j}_n = \frac{d}{dt}\int_{V_{\mathrm{obs}}} dV\rho_n,$$

and its time integration gives the associated nuclear yield

$$Y_n(t;A_{\mathrm{obs}}) = \int_0^t d\tau\, F_n(\tau;A_{\mathrm{obs}}).$$

In this case the nuclear flux can explicity be written as

$$F_n(t;A_{\mathrm{obs}}) = \frac{d}{dt}\int_0^{R_{\mathrm{obs}}} dR\rho_n(R,t). \tag{16}$$

IV. RESULTS AND DISCUSSIONS

The results presented in the following section show a good qualitative agreement of the fluxes obtained by solving the full molecular Schrödinger equation, Eq. (1), and by computing the BO wave function, Eq. (11). Our discussion puts the main focus

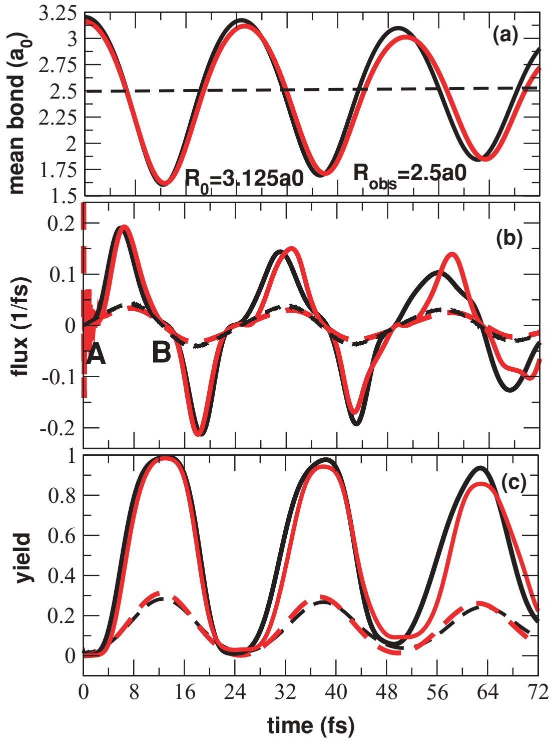

FIG. 3. (Color online) Dynamics for the outer initial condition centered in $R_1 = 3.125a_0$. The underlying simulations solve the full molecular Schrödinger equation [red (gray)] or use the BO approximation (black). Nuclear quantities are plotted by solid lines, electronic ones by dashed lines. (a) The mean bond length. Additionally, the observer location at $R_{\text{obs}} = 2.5a_0$ is indicated as a dashed horizontal line. The lower two panels show the evolution of the electronic and nuclear fluxes (b) and the yields (c). The dynamics within the regions marked by A and B are more thoroughly discussed in subsection IV B.

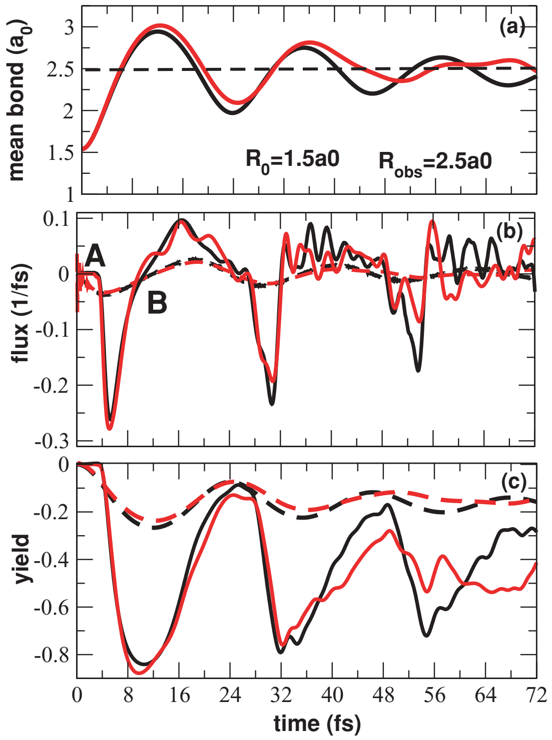

FIG. 4. (Color online) Dynamics for the inner initial condition centered in $R_2 = 1.5a_0$. The displayed quantities as well as their line encoding are the same as in Fig. 3.

on the oscillation pattern of the electronic and nuclear fluxes as well as their synchronicity. We also monitor electronic and nuclear dispersion for explaining part of the flux dynamics. Numerical aspects for the dynamics can be found in subsection 2 of the appendix.

A. Oscillation pattern

Figures 3 and 4 display results for the dynamics up to 72 fs. The initial wave functions are localized around the outer turning point $R_1 = 3.125a_0$ and the inner one $R_2 = 1.5a_0$, respectively. We compare results of the BO computations with the simulations based on the full molecular Schrödinger equation.

Figures 3(a) and 4(a) show the mean bond length $\langle R\rangle = \langle\Psi(r,z,R,t)|R|\Psi(r,z,R,t)\rangle$ as a function of time. The observer position at $R_{\text{obs}} = 2.5a_0$ is indicated by a dashed horizontal line. Figures 3(b), 4(b), 3(c) and 4(c) show both electronic and nuclear fluxes and the corresponding yields through the symmetric planes $z_{\text{obs}} = \pm R_{\text{obs}}/2$, respectively.

For the outer initial condition (Fig. 3), the nuclear yield reaches a maximum value of 1 around the inner turning point ($\langle R\rangle \approx 1.55a_0$ and $t \approx 12$ fs). The maximal electronic yield equals 0.32, which is less than 0.5. Hence the nuclei move almost completely from their initial location to the inner region, in contrast to the electron. After 12 fs, the nuclear yield gets slightly damped, while the electronic yield slowly oscillates with comparable amplitudes. The nuclear flux reaches its maximal value of 0.20 close to the equilibrium internuclear distance $R_{\text{eq}} = 2.0a_0$. The electronic flux shows a more regular oscillation pattern than the nuclear one.

For the inner initial condition (Fig. 4), the nuclear yield reaches a minimal value of approximately -0.8 around time $t = 12$ fs. The corresponding bond length is $\langle R\rangle \approx 3.0a_0$. After 24 fs, more vivid oscillations develop for both the nuclear yield and flux. These are fingerprints of quantum interference, due to the mixing of the nuclear fragments traveling back and forth. Since the initial slopes of the nuclear force, see Fig. 1(b), differ for the two initial conditions, the outer initial state does not generate a comparable interference pattern. One also notes that all the fluxes and yields in Fig. 4 are damped as time evolves. The electronic flux almost tends to zero, which is not the case in Fig. 3.

Our results are robust with respect to the location of the observer. Figure 5 shows the electronic and nuclear fluxes for both the outer [Fig. 5(a)] and the inner [Fig. 5(b)] initial conditions, at three different locations of the observer, $R_{\text{obs}} = 2.3a_0$, $2.4a_0$, and $2.5a_0$. The modulation of the fluxes and in particular the oscillation patterns persist when varying the observer position.

The flux computation via the full Schrödinger equation produces small high-frequency oscillations at the initial stage (within ≈3 fs), see the panels (b) in Figs. 3 and 4, respectively. This numerical artifact, associated with the BO initial wave function, has also been observed in the previous simulations for $H_2{}^+$ [13].

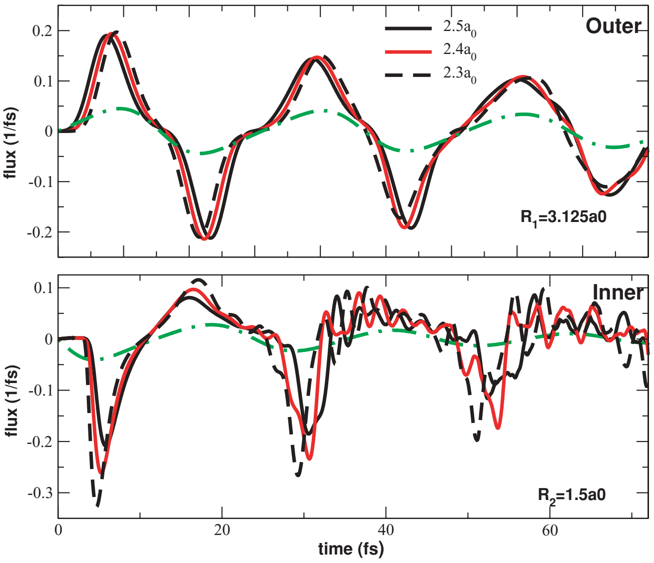

FIG. 5. (Color online) Robustness of the electronic and nuclear flux with respect to the observer position. The nuclear flux evolution for the outer and the inner initial state are shown in the upper and the lower panels, respectively. The three different locations of the observer are $R_{\rm obs} = 2.3a_0$ (dashed), $2.4a_0$ [red (gray)], and $2.5a_0$ (black). Both panels also plot the electronic flux (dot-dashed), which is insensitive to the considered variations of the observer plane.

B. Dispersion and synchronicity

We have also computed both the nuclear and the electronic dispersions:

$$\Delta R(t) = \left[\int dR\rho_n(R,t)(R-\langle R\rangle)^2\right]^{1/2}, \tag{17}$$

$$\Delta z(t) = \left[\int r dr\, dz\, \rho_e(r,z,t)(z-\langle z\rangle)^2\right]^{1/2}, \tag{18}$$

$$\Delta r(t) = \left[\int r dr\, dz\, \rho_e(r,z,t)(r-\langle r\rangle)^2\right]^{1/2}. \tag{19}$$

Figure 6 displays their time evolution for the outer initial condition (black lines) and the inner one (red/gray lines). Irrespective of the initial conditions, the electronic dispersion is in general larger than the nuclear one. For the first 3 fs, the nuclear dispersion for the inner initial condition decreases due to the wave function's location at the very steep wall. Afterward, it quickly increases and eventually reaches, as from 36 fs on, the strong electronic dispersion level. At this step, one may wonder why such strong oscillations mostly occur in the inner case and less in the outer one. To answer this question we first note that although the shapes of the initial wave packets for both cases are identical, with the same potential energy, their vibrational contents completely differ. Due to the steepness of the potential, the inner case contains more vibrational eigenstates than the outer one. During the propagation, the wave packet of inner case, superposition of many eigensates, exhibits a very pronounced dispersion (as already observed above) than the wave packet of the outer one. The increase of the nuclear dispersion for the inner initial state coincides with the irregular oscillations of the nuclear flux in Fig. 4(b). Also the different magnitudes of the nuclear and electronic yield in Fig. 3(c) can be linked with the different levels of the corresponding dispersion. Moreover, the electronic fluxes, yields, and dispersions all show a regular oscillation pattern.

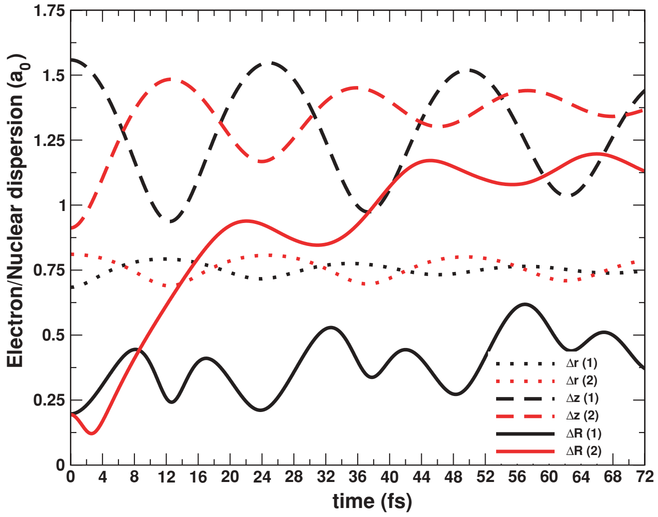

FIG. 6. (Color online) Electronic and nuclear dispersions as functions of time: the nuclear one $\Delta R(t)$ (solid), the electronic one in z direction $\Delta z(t)$ (dashed) and r direction $\Delta r(t)$ (dotted). The dynamics for the outer intial condition (1) are in black, while those for the inner one (2) are in [red (gray)] colors.

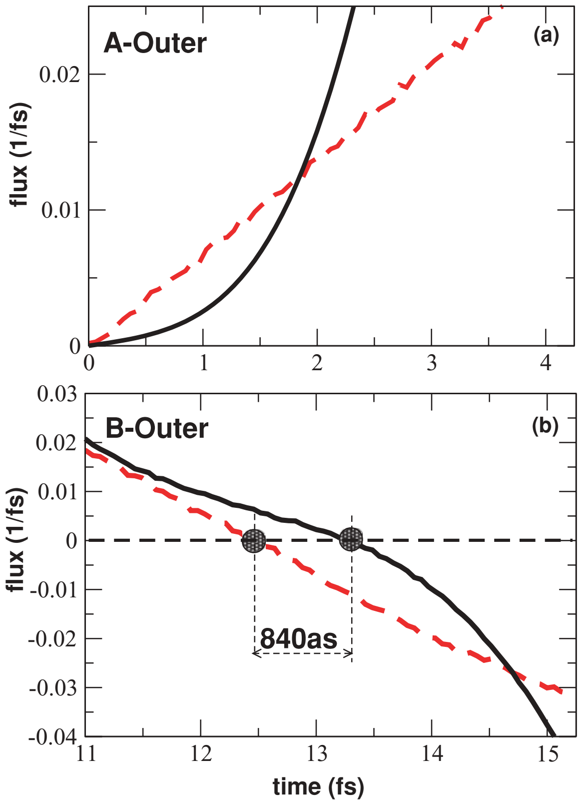

FIG. 7. (Color online) Enlargements of regions A and B of Fig. 3(b) for the nuclear flux (solid) and the electronic one (dashed). The electron and nuclei start moving synchronously (A-Outer). At later time (B-Outer), the electron returns first and after 840 as, the nuclei follow.

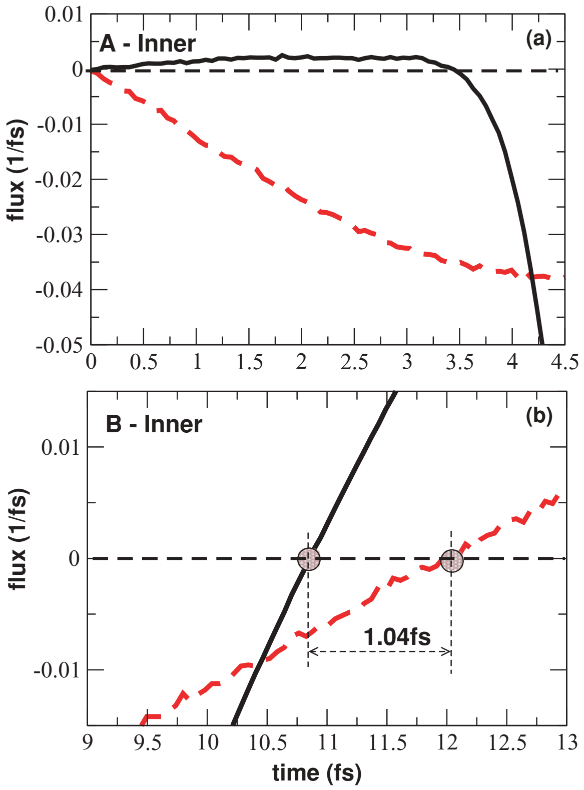

FIG. 8. (Color online) Enlargements of regions A and B of Fig. 4(b) for the nuclear flux (solid) and the electronic one (dashed). Until 3.5 fs, the electron and nuclei move in opposite directions (A-Inner). At later time (B-Inner), the nuclei return and the electron follows with a delay of 1.04 fs.

Analyzing the synchronicity of nuclear and electronic fluxes more closely, we have enlarged the regions A and B of the previous Figs. 3(b) and 4(b). For the outer starting condition (Fig. 7, A-Outer), the nuclei and the electron initially move in the same direction, while for the inner start (Fig. 8, A-Inner) both move in opposite directions for about 3.5 fs. Around the next turning point we also observe different behavior depending on the initial preparation. For the outer start (Fig. 7, B-Outer), the electron changes its direction before the nuclei with a time delay of 840 as, while for the inner start (Fig. 8, B-Inner) the electron effectively follows the nuclei with a time delay of 1.04 fs. The enlargements therefore illustrate that the light electron need not immediately adapt to the motion of the heavier nuclei.

V. SUMMARY AND CONCLUSION

The quantum evolution of coupled electronic and nuclear fluxes in an aligned deuterium molecular ion $D_2{}^+$ has been investigated, focusing on the initial state preparation. For large amplitude vibrational excitations, we show that the dynamics strongly depends on whether the process is initiated at the inner or at the outer turning points with respect to the equilibrium nuclear distance. Along these lines, the importance of such an initial state dependence on the generation of high harmonics has been demonstrated with a recent experiment on N_2O_4 molecules [14]. We believe that the presented theoretical work could motivate and eventually constitute a guide for experiments on coupled electronic and nuclear fluxes in a molecular model consisting of one-electron and two-nuclei such as $H_2{}^+$ and its isotopes.

Exploring the long time dynamics (72 fs) in more details, we found in particular that nuclear fluxes exhibit high-frequency oscillations for the inner turning point as initial condition. These oscillations are signatures of quantum interference that manifest as the mixing of nuclear wave packets traveling back and forth. Furthermore, we have identified attosecond intervals with surprising behavior. These intervals always occur close to the turning points where fluxes are small. It turns out that electrons need not always follow the nuclei as common intuition may predict.

The good agreement between the coupled fluxes computed either by the full molecular Schrödinger equation or by the BO approximation is encouraging and suggests the latter as a promising approach to tackle coupled electronic and nuclear fluxes in polyatomic molecules.

ACKNOWLEDGMENTS

We are very grateful to J. Manz for his valuable and stimulating discussions. Financial support by Freie Universität Berlin via the Center for Scientific Simulation as well as by Deutsche Forschungsgemeinschaft, Projects Sfb 450 TPC1 and TPC5, is gratefully acknowledged.

APPENDIX: NUMERICAL ASPECTS

1. Initial preparation

Using the GAUSSIAN 03 package [21] involving the configuration interaction single double (CISD) calculations with a correlation-consistent polarized basis set (aug-cc-pV5Z) [22], we solve the time-independent electronic Schroedinger Eq. (12). This provides us with the Potential Energy Surface of the electronic ground states of D_2 and $D_2{}^+$ as well as their corresponding electronic wave functions. The nuclear vibrational ground state of D_2 is subsequently promoted to the PES of $D_2{}^+$ and translated such that it is centered in $R_1 = 3.125a_0$ or $R_2 = 1.5a_0$.

2. Dynamics

The three-dimensional molecular Schrödinger equation, Eq. (1), has been solved by the method developed in Ref. [16]. The computations discretize the cylinder of radius $r_0 = 18.0a_0$ and height $2z_0 = 36a_0$ ($z \in [-z_0, +z_0]$) with 50 and 110 grid points, respectively. For the internuclear distance $R \in [0, 16.0a_0]$, 256 grid points have been used.

TABLE I. Time-averaged error of nuclear yield and flux. Numbers in brackets denote powers of 10.

	$R_1 = 1.5a_0$		$R_2 = 3.125a_0$	
Resolution	Yield	Flux	Yield	Flux
128	2.18[−3]	2.1[−6]	2.01[−3]	7.74[−7]
256	8.56[−5]	1.02[−7]	1.02[−4]	4.03[−8]
512	5.22[−6]	6.25[−9]	6.13[−6]	2.55[−9]
1024	3.0[−7]	3.57[−10]	3.6[−7]	1.58[−10]

The one-dimensional nuclear Schrödinger equation, Eq. (13), has been solved using the symmetrized splitting method together with the Fast Fourier transform [23,24]. An absorbing mask [25] has been used in order to avoid unphysical reflections at the boundary.

Moreover, we have performed a convergence study with respect to the nuclear flux and the yield. Table I collects the time averaged differences computed with varying resolution, while the reference value is obtained with 2048 grid points. The ratio of the 128-error over the 256-error is 25 for the yield and 20 for the flux. From 256 to 512 and from 512 to 1024 we have a convergence rate of about 16 for both. Therefore, our simulations use 256 grid points for the internuclear distance.

[1] A. Scrinzi, M. Y. Ivanov, R. Kienberger, and D. M. Villeneuve, J. Phys. B **39**, R1 (2006).

[2] M. F. Kling, Ch. Siedschlag, A. J. Verhoef, J. I. Khan, M. Schultze, Th. Uphues, Y. Ni, M. Uiberacker, M. Drescher, F. Krausz, and M. J. J. Vrakking, Science **312**, 246 (2006).

[3] P. B. Corkum and F. Krausz, Nature Phys. **3**, 381 (2007).

[4] F. Martín, J. Fernández, T. Havermeier, L. Foucar, Th. Weber, K. Kreidi, M. Schöffler, L. Schmidt, T. Jahnke, O. Jagutzki, A. Czasch, E. P. Benis, T. Osipov, A. L. Landers, A. Belkacem, M. H. Prior, H. Schmidt-Böcking, C. L. Cocke, and R. Dörner, Science **315**, 629 (2007).

[5] A. D. Bandrauk, S. Chelkowski, S. Kawai, and H. Lu, Phys. Rev. Lett. **101**, 153901 (2008).

[6] S. T. Park, A. Gahlmann, Y. He, J. S. Feenstra, and A. H. Zewail, Angew. Chem., Int. Ed. Engl. **47**, 9496 (2008).

[7] F. He, A. Becker, and U. Thumm, Phys. Rev. Lett. **101**, 213002 (2008).

[8] F. Krausz and M. Ivanov, Rev. Mod. Phys. **81**, 163 (2009).

[9] W. H. Miller, J. Chem. Phys. **61**, 1823 (1974); Acc. Chem. Res. **26**, 174 (1993); J. Phys. Chem. A **102**, 793 (1998).

[10] U. Manthe, T. Seideman, and W. H. Miller, J. Chem. Phys. **101**, 4759 (1994).

[11] T. Wu, H.-J. Werner, and U. Manthe, Science **306**, 2227 (2004).

[12] M. Okuyama and K. Takatsuka, Chem. Phys. Lett. **476**, 109 (2009).

[13] I. Barth, H.-C. Hege, H. Ikeda, A. Kenfack, M. Koppitz, J. Manz, F. Marquardt, and G. K. Paramonov, Chem. Phys. Lett. **481**, 118 (2009).

[14] W. Li, X. Zhou, R. Lock, S. Patchkovskii, A. Stolow, H. C. Kapteyn, and M. M. Murnane, Science **322**, 1207 (2008).

[15] D. Stalling, M. Westerhoff, and H.-C. Hege, in *The Visualization Handbook*, edited by Charles D. Hansen and Christopher R. Johnson (Elsevier, Amsterdam, 2005), Chap. 38, pp. 749–767.

[16] G. K. Paramonov, Chem. Phys. Lett. **411**, 350 (2005).

[17] S. Chelkowski, T. Zuo, O. Atabek, and A. D. Bandrauk, Phys. Rev. A **52**, 2977 (1995).

[18] L. S. Cederbaum, J. Chem. Phys. **128**, 124101 (2008).

[19] D. Geppert, P. von den Hoff, and R. de Vivie-Riedle, J. Phys. B **41**, 074006 (2008).

[20] M. Born and R. Oppenheimer, Ann. der Physik **84**, 457 (1927).

[21] M. J. Frisch, G. W. Trucks, H. B. Schlegel, G. E. Scuseria, M. A. Robb, J. R. Cheeseman, J. A. Montgomery Jr., T. Vreven, K. N. Kudin, J. C. Burant, J. M. Millam, S. S. Iyengar, J. Tomasi, V. Barone, B. Mennucci, M. Cossi, G. Scalmani, N. Rega, G. A. Petersson, H. Nakatsuji, M. Hada, M. Ehara, K. Toyota, R. Fukuda, J. Hasegawa, M. Ishida, T. Nakajima, Y. Honda, O. Kitao, H. Nakai, M. Klene, X. Li, J. E. Knox, H. P. Hratchian, J. B. Cross, V. Bakken, C. Adamo, J. Jaramillo, R. Gomperts, R. E. Stratmann, O. Yazyev, A. J. Austin, R. Cammi, C. Pomelli, J. W. Ochterski, P. Y. Ayala, K. Morokuma, G. A. Voth, P. Salvador, J. J. Dannenberg, V. G. Zakrzewski, S. Dapprich, A. D. Daniels, M. C. Strain, O. Farkas, D. K. Malick, A. D. Rabuck, K. Raghavachari, J. B. Foresman, J. V. Ortiz, Q. Cui, A. G. Baboul, S. Clifford, J. Cioslowski, B. B. Stefanov, G. Liu, A. Liashenko, P. Piskorz, I. Komaromi, R. L. Martin, D. J. Fox, T. Keith, M. A. Al Laham, C. Y. Peng, A. Nanayakkara, M. Challacombe, P. M. W. Gill, B. Johnson, W. Chen, M. W. Wong, C. Gonzalez, and J. A. Pople, GAUSSIAN 03, Revision C.02 (Gaussian, Inc., Wallingford CT, 2004).

[22] T. H. Dunning, J. Chem. Phys. **90**, 1007 (1989).

[23] M. D. Feit, J. A. Fleck, and A. Steiger, J. Comput. Phys. **47**, 412 (1993).

[24] C. Lubich, *Zurich Lectures in Advanced Mathematics* (European Mathematical Society, Zürich, 2008).

[25] A. Vibok and G. G. Balint-Kurti, J. Phys. Chem. **96**, 8712 (1992).